CHEMISTRY OF MATERIALS

pubs.acs.org/cm

Article

Control of Crystallization Pathways in the $BiFeO_3$–$Bi_2Fe_4O_9$ System

Andrea Kirsch,* Guilherme B. Strapasson, Niels Lefeld, Mathias Gogolin, Mark C. Videbæk, Soham Banerjee, Heloisa N. Bordallo, and Kirsten M. Ø. Jensen*

Cite This: https://doi.org/10.1021/acs.chemmater.4c02656

Read Online

ACCESS | Metrics & More | Article Recommendations | Supporting Information

ABSTRACT: Bismuth ferrites, specifically perovskite-type $BiFeO_3$ and mullite-type $Bi_2Fe_4O_9$, hold significant technological promise as catalysts, photovoltaics, and room-temperature multiferroics. However, challenges arise due to their frequent cocrystallization, particularly in the nanoregime, hindering the production of phase-pure materials. This study unveils a controlled sol–gel crystallization approach, elucidating the phase formation complexities in the bismuth ferrite oxide system by coupling thermochemical analysis and total scattering with pair distribution function analysis. We tune the crystallization pathways in the $BiFeO_3$–$Bi_2Fe_4O_9$ system by adjusting the metal to complexing agent ratio and pH during precursor preparation with a fixed Bi/Fe ratio of 1:2. Although all precursors undergo an amorphization process during heating, our results demonstrate a consistent correlation between the crystallization pathway and the initial structural entities formed during gel formation. Pair distribution function analysis reveals structural differences in the intermediate amorphous structures, which preferentially crystallize into either $BiFeO_3$ or $Bi_2Fe_4O_9$. This study offers mechanistic insights into the formation processes in the system and synthetic guidance for the controlled synthesis of pure $Bi_2Fe_4O_9$ and mixed $BiFeO_3/Bi_2Fe_4O_9$ nanomaterials. Additionally, it elucidates the unusual growth behavior and structural size dependence of $Bi_2Fe_4O_9$, particularly highlighting significant distortions in the local structure likely induced by the proximity of Bi's stereoactive lone electron pairs at small sizes.

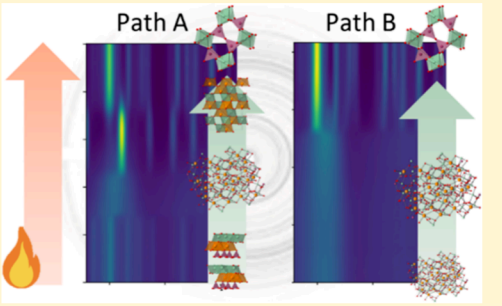

INTRODUCTION

The sol–gel method is a widely employed approach for synthesizing functional nanomaterials, involving the conversion of molecular precursors in a solution into inorganic solids through sequential hydrolysis, condensation, and aggregation processes.[1,2] Various factors, including the precursor type, pH, and the ratio between the metal precursor and the complexing agent, can influence the synthesis outcome.[3] In the initial stage, sol–gel processes often yield amorphous structures, which are crystallized through thermal treatments.[4] However, cocrystallization of competing thermodynamically stable or metastable phases can hinder the formation of single-phase materials, particularly within the temperature range used for producing nanomaterials. Although the strong impact of synthesis conditions in sol–gel processes is known and frequently explored heuristically, a majority of research focuses on obtaining pure compounds to deduce structure–property relationships. Few studies target a mechanistic understanding of synthesis and formation processes, and there are few reports of 'failed' synthesis outcomes.[5] This has led to a knowledge gap of valuable information regarding polymorphism, particle size, and microstrain that is crucial for designing materials tailored with specific properties.

Understanding the fundamental mechanisms behind material formation is central for guiding synthesis toward desired structures and properties.[6] Investigations of this nature, though infrequent, are essential, especially in systems prone to cocrystallization, polymorphism, and the formation of defective structures, given that even subtle variations in synthesis conditions can significantly impact the outcomes. Recent research has extensively explored materials formation, e.g., in hydrothermal synthesis, using both experimental[7,8] and theoretical[9,10] approaches. Particularly, pair distribution function (PDF) analysis has emerged as a valuable tool, which allows monitoring structural changes in both amorphous and crystalline phases throughout the entire formation process.[11,12]

The complex Bi_2O_3–Fe_2O_3 system has been extensively studied due to its well-known room-temperature multiferroic $BiFeO_3$ phase.[13−15] Despite many studies, the preparation of single-phase $BiFeO_3$ samples is still a challenge, and parasitic phases, such as $Bi_{25}FeO_{40}$, $Bi_2Fe_4O_9$, Bi_2O_3, Fe_3O_4, and Fe_2O_3, are often reported.[5,16,17] Independent of the starting stoichiometry, perovskite-type $BiFeO_3$ (Figure 1b) and mullite-type $Bi_2Fe_4O_9$ (Figure 1c) frequently cocrystallize, especially in the temperature range of ca. 450–770 °C, suggesting a small thermodynamic energy difference in the

Received: September 23, 2024
Revised: December 9, 2024
Accepted: December 9, 2024

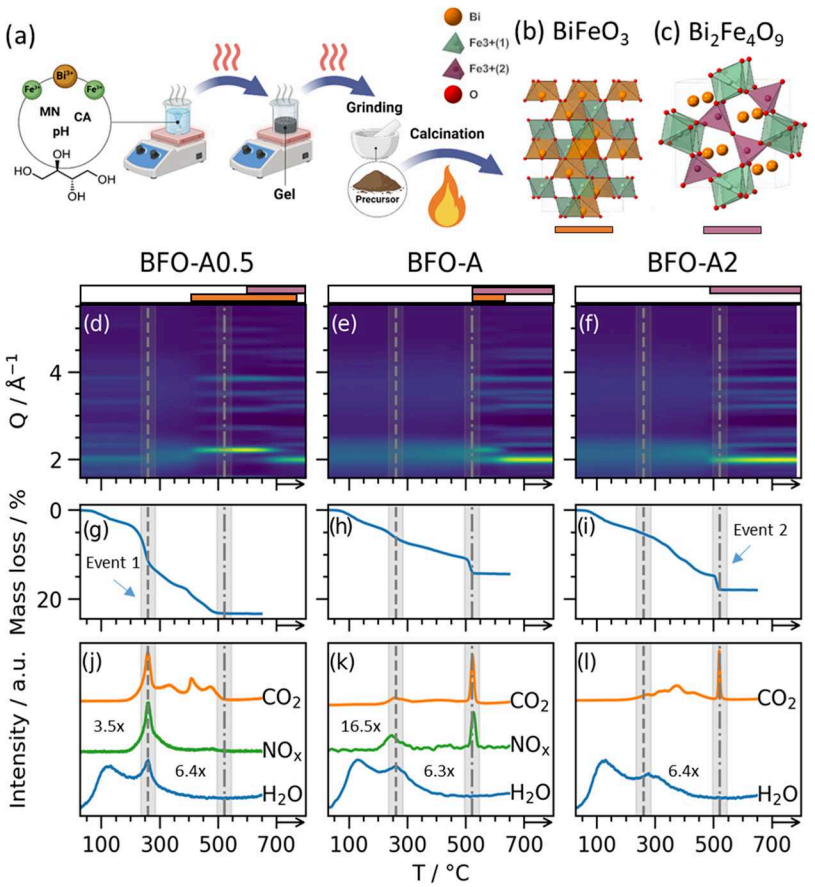

Figure 1. Synthesis and formation pathways of $BiFeO_3$ and $Bi_2Fe_4O_9$. (a) Schematic representation of the sol−gel synthesis employed in this study; varied parameters are the pH (acidic, neutral, basic) and molar metal nitrate (MN) to the complexing agent (CA) ratio. Structures of (b) perovskite-type $BiFeO_3$ and (c) mullite-type $Bi_2Fe_4O_9$. In situ total scattering patterns from room temperature to 700 °C for (d) BFO-A0.5 (MN/CA 1:0.375), (e) BFO-A (MN/CA 1:0.75), and (f) BFO-A2 (MN/CA 1:1.5) synthesized in acidic conditions (orange bars: $BiFeO_3$, pink bars: $Bi_2Fe_4O_9$). Evolution of the scale factors (Figure S3) and exemplary PDF fits (Figure S2) are displayed in the Supporting Information. Corresponding (g−i) mass losses and (j−l) H_2O, CO_2, and NO_x evolution during calcination from room temperature to 650 °C, as determined by TGA-MS. The dot−dashed lines highlight the breakdown of the crystalline precursor in sample BFO-A0.5 (Event 1) and crystallization of $Bi_2Fe_4O_9$ in BFO-A2 (Event 2). Note the different magnifications for the gas releases.

formation enthalpy between these phases.[5,18,19] $Bi_2Fe_4O_9$ has received considerably less attention compared to $BiFeO_3$, although it possesses interesting magnetic,[20] electronic,[21] optical,[22] photoelectrochemical,[23] and multiferroic[24] properties close to room temperature. The structure exhibits two distinct Fe sites forming a Cairo pentagonal magnetic lattice, in which geometrical frustration is interlocked with complex connectivity and hierarchical exchange interactions.[20,25] Studies on a series of nanocrystalline samples from 35 to 400 nm indicated a rotation of the magnetic spins due to distortions of the FeO_6 and FeO_4 polyhedral coordination below a critical size of 121 nm.[26] Additionally, size-dependent photocatalytic,[22] ferroelectric,[27] and magnetic properties[28,29] for $Bi_2Fe_4O_9$ and $BiFeO_3$ have been reported. Thus, precise control of the structure and size is essential in the synthesis of these materials.

In our study, we investigate how the synthesis parameters affect the crystallization pathways of $Bi_2Fe_4O_9$ and $BiFeO_3$ in a sol−gel process. By adjusting the pH and the ratio of metal precursor to complexing agent, we synthesized five different precursors with a Bi/Fe 1:2 stoichiometry. We followed their transformation into fully crystalline structures at higher temperatures by using PDF analysis of in situ total scattering (TS) data. This allowed us to investigate the crystallization process of bismuth ferrite oxide systems in depth, understand the mechanisms leading to the formation of $BiFeO_3$ and $Bi_2Fe_4O_9$, and reveal the nature of $Bi_2Fe_4O_9$ unusual growth and size-dependent behavior.

We show that precursor preparation under different synthesis conditions fundamentally changes the crystallization behavior at higher temperatures. By adjusting the pH and complexing agent amount, we can control the crystallization process, leading to various outcomes including (i) initial formation of $BiFeO_3$ followed by transformation into $Bi_2Fe_4O_9$, (ii) cocrystallization of $BiFeO_3$ and $Bi_2Fe_4O_9$, or (iii) direct formation of $Bi_2Fe_4O_9$. Despite all samples passing through an amorphous state, we observe a clear correlation between the structural entities formed during gel formation and the subsequent crystallization pathway. Moreover, these intermediate amorphous structures have distinct structural characteristics and preferentially crystallize into either $BiFeO_3$ or $Bi_2Fe_4O_9$.

A detailed investigation of the direct crystallization pathway to $Bi_2Fe_4O_9$ reveals significant distortions in the local structure likely induced by the close proximity of Bi's stereoactive lone electron pair at small sizes. This finding might explain the previously observed size-dependent properties and structural instabilities at small sizes in this system.

https://doi.org/10.1021/acs.chemmater.4c02656
Chem. Mater. XXXX, XXX, XXX−XXX

The results of our mechanistic study are manifold and highlight the importance of material formation studies. First, it offers synthetic guidance for bismuth ferrite materials, including the synthesis of single-phase $Bi_2Fe_4O_9$ nanomaterials or $BiFeO_3/Bi_2Fe_4O_9$ nanocomposites. Second, it reveals the relationship between structural features and growth dynamics in $Bi_2Fe_4O_9$, unveiling intriguing phenomena at the nanoscale. Lastly, it demonstrates that metal−carbohydrate complexes might be used as tailored precursor materials to strategically design crystallization processes for functional inorganic materials.

EXPERIMENTAL SECTION

Synthesis. The samples were synthesized by using the sol−gel approach. First, 5 mmol $Bi(NO_3)_3{\cdot}5H_2O$ (reagent grade, 98% Sigma-Aldrich), 10 mmol $Fe(NO_3)_3{\cdot}9H_2O$ (reagent grade, 98% Sigma-Aldrich), and complexing agent (meso-erythritol, ≥99% Sigma-Aldrich) are dissolved in deionized water. In a second step, the pH is adjusted using either 4 M NaOH (ACS reagent, ≥97.0%, pellets Sigma-Aldrich) or conc. HNO_3 (TraceSELECT for trace analysis, >69.0, Honeywell). Heating the solution under stirring to 100 °C for about 1.5 h leads to a gel, which is subsequently heated at 200 °C for 18 h to remove residual organics and obtain a solid powdered precursor. This is ground and used for the in situ experiments. The sample synthesized under basic conditions (BFO-B) was washed with deionized H_2O until neutral before heating to remove any remaining NaOH, which would degrade the quartz capillaries during the high-temperature experiments. Relevant synthesis parameters are given in detail in Table 1.

Table 1. Synthesis Conditions of the Five Precursors and Their Respective Sample Names

sample name	pH media	molar ratio MN/CA[a]	volume 4 M NaOH or conc. HNO_3/mL	volume H_2O/mL
BFO-B	basic (NaOH)	1:0.75	2	27.5
BFO-N	neutral	1:0.75		27.5
BFO-A	acidic (HNO_3)	1:0.75	3	27.5
BFO-A0.5	acidic (HNO_3)	1:0.375	1.5	13.7
BFO-A2	acidic (HNO_3)	1:1.5	6	55

[a]Metal nitrate:complexing agent (MN/CA) ratio with meso-erythritol as the complexing agent.

It is crucial to emphasize that the material labeled as "gel" may be in fact a dry foam, dry powder, or gel-like material, depending on the synthesis conditions and starting materials used. We use the term "gel" solely to refer to the stage of the synthesis, which is frequently used in the literature.

X-ray Diffraction and Total Scattering. In situ X-ray diffraction data were collected at P21.1 at PETRA III/DESY in Hamburg, Germany, using a wavelength of 0.12203 Å and a PerkinElmer XRD 1621 flat panel detector with a sample detector distance of ca. 500 mm. The powder samples were placed in an open quartz capillary in a horizontal position. The capillary was only half filled and left open at one end to allow for gas exchange. The powder was held in place by using quartz wool. The temperature was increased using a heating fan and a heating rate of 20 K min^{-1}. For the crystallization experiments, the samples were heated from room temperature to 700 °C and kept for ca. 1−2 h.

In contrast to conventional X-ray diffraction (XRD) and the refinement of the average structure, a PDF gives access to the local structure of the materials, as all scattering of the sample is considered in the analysis. Also, the diffuse scattering, whose information is usually discarded as background in conventional Rietveld refinements, is taken into account. The reduced PDF ($G(r)$) is obtained by a Fourier transform of the reduced total scattering structure function (FQ)

$$G(r) = \frac{2}{\pi}\int_{Q\,min}^{Q\,max} F(Q)\sin(Qr)\mathrm{d}Q \tag{1}$$

This function is obtained from the total scattering data ($I(Q)$) subtracted by the scattering of the background quartz capillary and divided by the number of scatterers N and the average scattering power per atom $\langle f(Q)\rangle^2$ to amplify scattering at high-Q (SQ)

$$F(Q) = Q(S(Q) - 1) \tag{2}$$

$$S(Q) = \frac{1}{N\langle f\rangle^2}(I(Q) + \langle f\rangle^2 - \langle f^2\rangle) \tag{3}$$

The PDF resembles atom−atom pair correlations in the material and allows for individual refinement of local and average structures as well as a model-free analysis of structural changes. PDFs were generated with a Qmax Inst of 25 $Å^{-1}$, Qmax 21.465 (in situ), and Qmax 19.6 (ex situ). Data was collected with a time resolution of 5 s. The PDFs shown in Figure 2f−h were summed over 50 s to reduce the noise due to a low scattering signal.

Refinement Strategy. The in situ data was refined using PDFgui. Since BFO-A and BFO-A0.5 show regimes with different crystal structures present, we divided the data sets into regions, where the relevant phases were refined as shown in Figure S0 to generate the plots shown in Figure S3. Exemplary fits are shown in Figure S2. Refined parameters include the scale factor of the respective phases ($BiFeO_3$ and $Bi_2Fe_4O_9$, if present), lattice parameters a, b, c ($Bi_2Fe_4O_9$) and a, c ($BiFeO_3$), sp-diameter to account for the dampening due to small crystallite sizes, atomic positions of Bi, and isotropic atomic displacement parameters (ADP) grouped by the atom type.

More sophisticated data analysis was performed for sample BFO-A2, which only forms $Bi_2Fe_4O_9$. We performed a reverse sequential refinement by including only the region 15−60 Å. By that, we could exclude fitting artifacts stemming from the precursor as it shows only atom-pair correlations up to 15 Å. Refined parameters include the scale factor, lattice parameters a, b, c, and sp-diameter (only up to 629 °C, as from there the parameter took unreasonable values since the crystallites were too big (~40 nm)), atomic positions of Bi and Fe, and isotropic ADPs grouped by the atom type for Fe and O. The Bi ADPs were refined anisotropically. The refined parameters are shown in Figures S21 and 4a−c. Exemplary fits are shown in Figures S2a and 4d−f.

FTIR. Attenuated total reflectance Fourier transform infrared (FTIR) spectroscopy measurements were conducted in an Agilent Cary 630 FTIR spectrometer, in the 4000−500 cm^{-1} range, with a resolution of 4 cm^{-1}; 64 scans were collected for signal accumulation. Measurements of BFO-A0.5, BFO-A, BFO-A2, BFO-N, and BFO-B were acquired, as well as the as-received m-erythritol and m-erythritol under different media, i.e., acidic, neutral, and alkaline. For the preparation of m-erythritol under different media, the same procedure of the sample precursor preparation was employed in the absence of any metal. All samples were measured in powder form.

Coupled TGA/MS/IR. Thermogravimetric analysis coupled with mass spectrometry and infrared spectroscopy (TGA/MS/IR) were acquired in a TG 209 F1 Libra PERSEUS from NETZSCH attached to a MS (QMS403C Aeolos, Netzsch) and a FTIR (Bruker Optics). The measurements were conducted under synthetic air flow (20% O_2/80% N_2; 20 mL min^{-1}), with a heating rate of 20 °C min^{-1}, up to 650 °C. Around 3 mg of each sample was placed in a Al_2O_3 crucible, and instrument correction was performed on an empty crucible before starting the measurements. MS and IR data were acquired simultaneously with TGA. IR spectra were each collected for 3 min in the gas phase. MS data was presented taking into account the higher-intensity m/z fragment that did not overlap with any other product. The temperatures of the mass loss events were determined by the maximum of the first derivative of the respective TGA data.

https://doi.org/10.1021/acs.chemmater.4c02656
Chem. Mater. XXXX, XXX, XXX−XXX

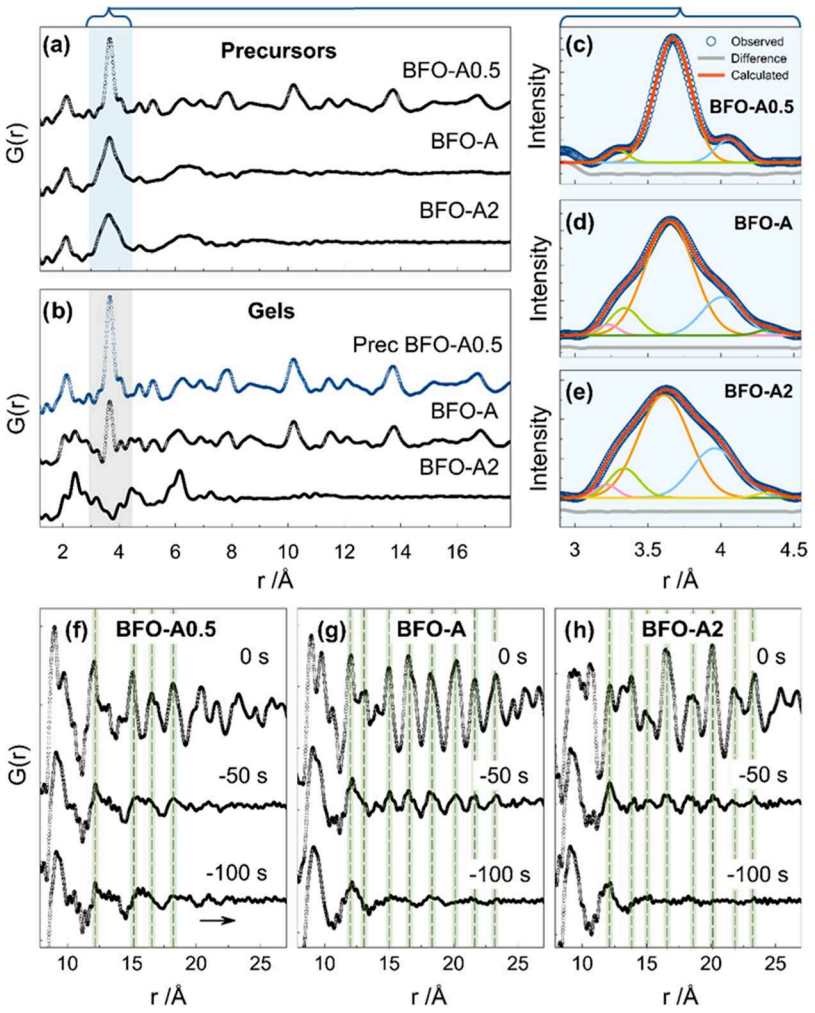

Figure 2. Pair distribution functions (PDF) of (a) precursors and (b) gels of samples BFO-A2 (MN/CA 1:1.5), BFO-A (MN/CA 1:0.75), and BFO-A0.5 (MN/CA 1:0.375) synthesized in acidic conditions. The blue box in panel (a) highlights the range that is magnified in panels (c–e). The gray box in panel (b) highlights the missing metal–metal distances at ca. 3.7 Å in the gel BFO-A2 PDF typical for metal oxides. (c–e) Magnified low-r region of PDFs shown in panel (a) fitted by Gaussians. PDFs at the point of crystallization (t = 0 s) and before (t = −50 s and t = −100 s) for (f) BFO-A0.5, (g) BFO-A, and (h) BFO-A2. The dotted lines serve as a guide for the eye to demonstrate the similarity of peaks between the PDFs at different stages of crystallization. The arrow in panel (f) highlights the higher correlation lengths compared to the PDF at t = −50 s.

RESULTS AND DISCUSSION

Overview of Crystallization Pathways. We investigate the impact of metal nitrate (MN) to complexing agent (CA) ratios on the sol–gel synthesis of multiferroic $Bi_2Fe_4O_9$ and $BiFeO_3$, using *m*-erythritol as the CA (Figure 1a–c). Powder precursors were synthesized, and their crystallization during calcination (room temperature to 700 °C) was monitored using in situ X-ray TS and PDF analysis. With a constant Bi:Fe stoichiometry (1:2 at.), we varied the MN/CA ratio in acidic media, analyzing three precursors in depth: BFO-A0.5 (MN/CA of 1:0.375), BFO-A (MN/CA of 1:0.75), and BFO-A2 (MN/CA of 1:1.5). For comparison, we additionally prepared two precursors under different media—alkaline (BFO-B) and neutral (BFO-N)—while maintaining a constant MN/CA ratio of 1:0.75. A list of the five precursors prepared can be found in Table 1.

We first focus on the three samples synthesized in acidic media and establish an overview of the reaction processes. In situ TS during calcination revealed different crystallization pathways for the three samples (Figure 1d–f). (i) The BFO-A0.5 precursor (higher MN/CA ratio) initially is crystalline but collapses into an amorphous phase at 275 °C (Figures 1d and S1c). $BiFeO_3$ forms as the only crystalline phase at 410 °C, while mullite-type $Bi_2Fe_4O_9$ crystallization starts at 620 °C, suggesting that some iron is present as an amorphous phase in the first crystallization step. Single-phase $Bi_2Fe_4O_9$ formed after 6 min at 700 °C (Figures S1c, S2c, and S3c). (ii) The BFO-A precursor (intermediate MN/CA ratio) initially is amorphous and crystallizes into a $BiFeO_3/Bi_2Fe_4O_9$ mixture at 506 °C, while single-phase $Bi_2Fe_4O_9$ is achieved at 645 °C (Figures 1e, S1b, S2b, and S3b). (iii) The amorphous BFO-A2 precursor (lower MN/CA ratio) directly crystallizes into single-phase $Bi_2Fe_4O_9$ at 512 °C (Figures 1f, S1a, and S2a). Selected scattering patterns, PDF fits, and quantitative phase content evolution of the crystallization processes are given in Figures S1, S2, and S3. All three samples ultimately yielded single-phase $Bi_2Fe_4O_9$, however, at different temperatures: BFO-A2 (512 °C) < BFO-A (645 °C) < BFO-A0.5 (700 °C/6 min). We observe a clear correlation with the MN/CA ratio, where a

https://doi.org/10.1021/acs.chemmater.4c02656
Chem. Mater. XXXX, XXX, XXX–XXX

higher CA (m-erythritol) content significantly accelerates $Bi_2Fe_4O_9$ crystallization.

Due to the nature of the sol−gel process, which involves the use of molecular starting materials and organic complexing agents, the release of small molecules during calcination is expected. Thus, to obtain thermochemical insights into the formation process, we performed thermogravimetric analysis (TGA) coupled with Fourier transform infrared spectroscopy (FTIR) and mass spectrometry (MS) under conditions comparable to those in the TS experiments (Figures 1g−l (TGA/MS) and S4−S6 (FTIR)). During heat treatment, the samples release H_2O (blue curves), CO_2 (orange curves), and NO_x (green curves) in varying amounts. All samples show comparable H_2O evolution of ∼4% until 200 °C (Figure 1g−l). This is interesting since the samples were already preheated at 200 °C for 18 h during precursor preparation, which suggests that the samples display a reversible water uptake/loss process. After 200 °C, CO_2 and NO_x releases start and align very well with the phase transitions observed in the TS data (Figure 1d−f). For simplicity, we will discuss the data with regard to the occurrence of two significant events: the breakdown of the crystalline precursor in sample BFO-A0.5 (Figure 1g, Event 1, dashed line) and the crystallization of $Bi_2Fe_4O_9$ in sample BFO-A2 (Figure 1i, Event 2, dashed line).

We again first consider BFO-A0.5. At 250 °C (Figure 1g, dashed line), a steep mass loss of 12.9% is accompanied by simultaneous evolution of H_2O, CO_2, and NO_x (Figure 1j). This event directly correlates with the amorphization of the initially crystalline precursor (Figure 1d, Event 1). Subsequently, gradual mass loss of 7.5% and multistep CO_2 evolution coincides with $BiFeO_3$ crystallization, with no further mass loss or gas evolution observed after 520 °C (Figure 1j, dot−dashed line). In contrast, BFO-A2 shows a gradual mass loss of ∼15% until 500 °C, concomitantly releasing H_2O and CO_2 in a multistep process with broad features (Figure 1i,l). This is followed by a sharp mass loss of 3.4% and a major CO_2 release, which correlates to the crystallization of $Bi_2Fe_4O_9$ in the TS data (Figure 1f, Event 2). While samples BFO-A2 and BFO-A0.5 show very different thermochemical behaviors, BFO-A shows features of both samples (Figures 1h,k and S7). As observed for BFO-A2, BFO-A shows a gradual mass loss of ∼11% until ∼500 °C, followed by a sharp mass loss of 3.6% with simultaneous release of CO_2 (Figure 1h,k). At the same time, a small but sharp release related to NO_x appears for BFO-A, which is absent for BFO-A2 and will be discussed below. The sharp gas release signals align well with the cocrystallization of $BiFeO_3$ and $Bi_2Fe_4O_9$ (Figure 1e,k, Event 2). At 250 °C, we observe a concomitant release of H_2O, CO_2, and NO_x comparable to BFO-A0.5, albeit in significantly lower quantities (Figure 1k, mass loss: 12.9% (BFO-A0.5) vs 4% (BFO-A)). This observation may imply that the molecular entity found for BFO-A0.5 is also present in BFO-A, however, in smaller amounts. Interestingly, the temperatures of gas releases associated with the breakdown of the crystalline precursor in BFO-A0.5 (Event 1) and the crystallization of $Bi_2Fe_4O_9$ in BFO-A2 (Event 2), exactly match the ones observed for BFO-A (Figure S7d). This suggests that BFO-A is a mixture of two molecular species (BFO-A2 + BFO-A0.5) with a very distinct thermochemical behavior. This is a surprising and exciting result, especially when considering that BFO-A crystallizes into a mixture of $BiFeO_3$ and $Bi_2Fe_4O_9$, while the other samples first crystallize into either $Bi_2Fe_4O_9$ or $BiFeO_3$ (Figure 1d−f). A summary of the mass losses and temperatures for Events 1 and 2 is presented in Table S1.

BFO-A0.5 and BFO-A both evolve NO_x during heating, while BFO-A2 does not, although a constant amount of metal nitrate (MN) is used in all syntheses. The quantity of NO_x species correlates well with the MN/CA ratio, where higher ratios lead to an increased rate of NO_x evolution. This observation suggests that the −OH groups of m-erythritol (Figures 1a and S16) strongly coordinate to the metal centers. With a higher MN/CA ratio, there is insufficient CA to saturate the metal centers and NO_3^- coordinates instead. The presence of NO_3^- in both BFO-A0.5 and BFO-A precursors is supported by bands at 1352 and 1310 cm^{-1} in the FTIR spectra (Figure S8).[30,31] BFO-A2 is synthesized with a higher CA content. During the precursor preparation, dissolved NO_3^- already evolves as NO_x species as evidenced by the release of orange/brownish vapors. This observation aligns with the well-documented strong complexation capability of various sugar alcohols with diverse metal centers, including *m*-erythritol.[32] Pure m-erythritol is known to decompose at temperatures below 350 °C.[33] Samples BFO-A and BFO-A2 show notably high combustion temperatures of ∼500 °C (Figures 1k,l and S7) for carbonaceous content. This suggests that carbon (and small amounts of nitrogen in the case of BFO-A; see Figures 1k and S7b) is integrated within the amorphous precursor structures. To support this hypothesis, we observed darkening of the samples during the in situ TS experiments at high temperatures (∼500 °C). Shortly after, the samples turned lighter again, followed by immediate crystallization of the samples, which was evident from the formation of clear powder rings on the detector. We associate the appearance of the dark color with segregation of carbon from the amorphous structure, subsequently oxidizing into CO_2, as confirmed by TGA-MS data (Figure 1j−l).

The results of our combined study unequivocally show a strong connection between the observed crystallization events and the evolution of gases from the precursors with very distinct temperatures. These findings highlight the role of the precursor in the full crystallization process in a sol−gel synthesis.

Structural Analysis of Precursors. Having obtained an overview of the crystallization processes, we now aim to gain a deeper understanding of the factors influencing the distinctive crystallization pathways. We thus conduct detailed XRD and PDF analyses on samples at two critical stages in the synthesis process, here referred to as the "gel" and "precursor" (Figure 1a). Gel refers to the stage after solvent evaporation at 100 °C for 1.5 h, while the precursor refers to the product obtained after heat-treating the sample at 200 °C for 18 h, as described in the Experimental Section.

We initially focused on the crystalline precursor structure of BFO-A0.5. The XRD pattern shows intense Bragg reflections at low diffraction angles, e.g., $2\theta = 10.9°$ as seen in Figures S9b and S10, indicating a large unit cell. Given the presence of NO_3^- and H_2O in the sample (MS, FTIR; Figures 1j, S7c, and S8), we tried fitting the data with known bismuth and iron nitrates/oxyhydroxy nitrates, however, without success (Figure S10). Considering the flexibility of bismuth-containing molecular materials, varying in size, symmetry, and content of small molecules,[34] it is plausible that the structure might still be unknown.

In contrast to crystalline BFO-A0.5, the XRD patterns of the BFO-A and BFO-A2 precursors show broad bumps, character-

https://doi.org/10.1021/acs.chemmater.4c02656
Chem. Mater. XXXX, XXX, XXX−XXX

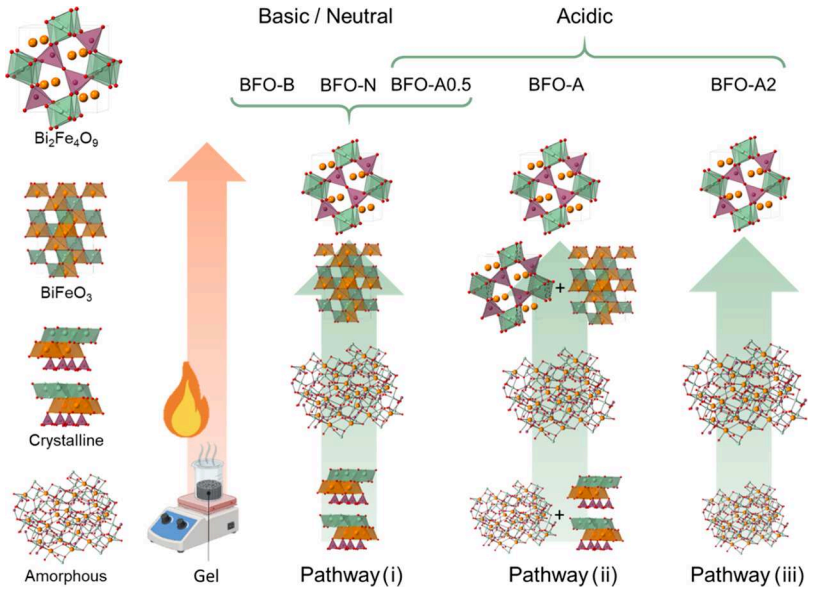

Figure 3. Overview of the Crystallization Pathways of the samples in this study. For synthesis conditions, refer Table 1. The phases referred to as "crystalline" and "amorphous" in the figure are just visual representatives and do not describe explicitly determined structures.

istic of amorphous materials (Figure S9b). We therefore turn to the analysis of their PDFs. These contain details about atom−atom distances within the sample, thereby allowing the characterization of both crystalline and noncrystalline materials. Although we generalize metal−metal distributions in the sample as Bi−Bi, since the signal is dominated by scattering of Bi, Bi−Fe and Fe−Fe contributions will also contribute to the PDFs. The precursor PDFs for BFO-A0.5, BFO-A, and BFO-A2 are shown in Figures 2a and S11b. BFO-A0.5 shows very distinct structural features to high *r*-values, as expected for crystalline samples. In contrast, no clear atom-pair correlations are evident beyond 5 Å for BFO-A and BFO-A2. Instead, the PDFs show broad oscillations extending to approximately 12 Å, a characteristic typical for amorphous materials. All three samples show peaks with maxima at 2.1 and 3.7 Å, which align with typical metal−oxygen (M−O) and metal−metal (M−M) distances for Bi−O and Bi−Bi.[35] While the Bi−Bi peak at 3.7 Å is sharp for crystalline BFO-A0.5, it is broad for BFO-A and even broader for BFO-A2. Fitting this peak requires three Gaussian components for BFO-A0.5 (Figure 2c), but five are needed for BFO-A (Figure 2d) and six for BFO-A2 (Figure 2e). This implies that BFO-A0.5 has a well-defined Bi−Bi environment. Indeed, complementary FTIR measurements show a narrow absorption band at 798 cm^{-1} for BFO-A0.5 (Figure S8), indicative of distinct metal−oxygen bonds, which are expected for an ordered crystalline structure. In contrast, this sharp band is absent for BFO-A and BFO-A2, which aligns well with the broad distribution of Bi−Bi distances observed in their PDFs (Figure 2d,e). While a broad distribution of M−O and M−M distances is expected for amorphous materials, a clear difference in this distribution for samples BFO-A and BFO-A2 is evident. BFO-A shows a sharper feature at 3.7 Å (Figure 2d), and therefore a narrower Bi−Bi distribution, than BFO-A2 (Figure 2e). This suggests that BFO-A and BFO-A2 have, at least in parts, different structures, although both samples are amorphous (Figure S9b). Interestingly, the PDF of BFO-A shows some weak structural features, which can also be seen for BFO-A0.5, e.g., at 10 and 13.5 Å (see arrows in Figure S12). This suggests that BFO-A represents a mixture of BFO-A2 and BFO-A0.5 comparable to the results from the previous section.

Structural Analysis of Gels. We additionally investigate the structures of the "gels", i.e., the samples obtained *before* the heating step at 200 °C (Figure 1a). We compared the gel PDFs in Figure 2b. The sticky nature of the BFO-A0.5 sample precluded us from obtaining a sample suitable for scattering experiments; however, we are able to compare the BFO-A and BFO-A2 gels to the BFO-A0.5 precursor, as discussed below. The most obvious differences among the three samples are the correlation lengths of the structural features in the PDF. BFO-A2 shows correlations only up to about 8 Å, suggesting its coherence length is very small, while BFO-A is crystalline. Surprisingly, a pronounced similarity is evident between the BFO-A gel and the BFO-A0.5 precursor PDFs, which are practically identical from $r > 7$ Å (Figure 2b). The two samples also show similar XRD patterns (Figure S9a). The PDFs differ in the local range from r = 1.3 Å − 7 Å, as highlighted by the gray region in Figure 2b. While a sharp PDF peak is seen at 3.7 Å for both samples, it is less intense in the BFO-A gel. BFO-A furthermore displays atom-pair correlations absent in BFO-A0.5, such as at 2.4, 2.8, and 4.5 Å (Figures 2b and S13). Interestingly, the same peaks are present in the BFO-A2 gel, which again suggests that BFO-A is composed of a mixture of the structures observed in BFO-A2 and BFO-A0.5.

To obtain further insight, we analyze the structure of the BFO-A2 gel more thoroughly. The BFO-A2 gel presents very distinct distances at 2.4, 2.8, and 4.5 Å but no correlation lengths above 7.5 Å (Figures 2b and S11a). The first two peaks fit to the bond lengths of typical Bi−O/Fe−O coordination. However, we cannot observe a peak for typical Bi−Bi, Bi−Fe, or Fe−Fe distances, which usually would be a strong peak at ca. 3−4 Å in metal oxides (e.g., the peak at 3.7 Å for BFO-A and BFO-0.5 in Figure 2a,b). This led us to hypothesize that the BFO-A2 gel structure could be a molecular entity. As such, we have searched the literature for known metal−m-erythritol complexes and found a range of these, including lanthanide−erythritol complexes.[31,36] These compounds have several configurations, where m-erythritol differently complexes the

https://doi.org/10.1021/acs.chemmater.4c02656
Chem. Mater. XXXX, XXX, XXX−XXX

metal cations.[31,36] We have picked several representatives of those (Figure S14), calculated their theoretical PDFs, and compared them to our BFO-A2 sample (Figure S15a). Similar to the PDF of our sample, none of the PDFs of the lanthanide−erythritol complexes shows the typical M−M distance known for metal oxides (Figure S15a, dashed line).

The M−M distances between the single units of these molecular crystals range from 6.7 to 7.8 Å. For our sample, we estimate M−M distances of ∼5.5−6.5 Å, where we observe two peaks in the PDF. The simulated PDFs of the lanthanide−erythritol complexes show qualitatively comparable atomic pair distances to our sample at low r (2−4 Å). Hence, we propose that the distinguishable peaks in the PDF of our sample can be attributed to Bi/Fe−O, Bi/Fe−N, and Bi/Fe−C, as deduced from the simulated partial PDFs from a lanthanide/erythtritol complex (Figure S15b). In contrast to these complexes, our sample is not an ordered molecular crystal. Therefore, we cannot observe any PDF peaks beyond ∼7 Å, as randomization of the complexes would cause a strong dampening of the PDF. Here, we speculate that we form a Bi/Fe−erythritol complex in the first step in the synthesis of BFO-A2. However, further investigations would be needed for confirmation, which is beyond the scope of this work.

Surprisingly, we can correlate the crystallization pathway with the gel structures formed in the initial step of the synthesis during solvent evaporation. This implies that they significantly impact or directly dictate the crystallization pathway at high temperatures. This is a remarkable finding, as all samples pass through an amorphous intermediate state during heating (Figure 1d−f). This hypothesis gains further support when considering the crystallization pathways of samples BFO-B and BFO-N, which were synthesized with the MN/CA ratio of BFO-A, but under basic (BFO-B) and neutral (BFO-N) conditions (Table 1). Although synthesized in different pH media and with different MN/CA ratios, they exhibit a crystallization path akin to BFO-A0.5 (Figure S16). When considering PDFs and XRDs from their gels (Figures S9a and S11a), we furthermore see the same crystalline phase identified in the BFO-A gel and the BFO-A0.5 precursor (Figure S9a). An overview of the established crystallization pathways is given in Figure 3. In summary, (i) samples displaying a similar crystalline phase in the gel PDF, such as BFO-A0.5, BFO-B, and BFO-N, crystallize initially into the $BiFeO_3$ structure, later transforming into $Bi_2Fe_4O_9$. (ii) BFO-A, representing a mix of both structures in the gel, simultaneously crystallizes into a mixture of $BiFeO_3$ and $Bi_2Fe_4O_9$. (iii) BFO-A2, with a distinctly different gel PDF, crystallizes directly into $Bi_2Fe_4O_9$ without forming the $BiFeO_3$ intermediate structure.

Structural Changes at the Point of Crystallization: From "Amorphous" to Crystalline. To get a deeper understanding of the crystallization process, we now have a closer look into the PDFs of BFO-A0.5, BFO-A, and BFO-A2 just at the point of crystallization (t = 0 s) and before (t = −50 and −100 s). The time stamps are determined from the point when the first clear reflections appear in the Q-space data (Figures 1d−f and S17). The PDFs are shown in Figure 2f−h. At t = 0 s, BFO-A2 shows significantly different atomic pair distances compared to BFO-A0.5. From the PDFs calculated from the crystal structures of $BiFeO_3$ and $Bi_2Fe_4O_9$, it is evident that BFO-A0.5 already shows the main atom-pair correlations of $BiFeO_3$ and BFO-A2, the ones of $Bi_2Fe_4O_9$ (see arrows in Figure S18). Again, while BFO-A0.5 and BFO-A2 seem to represent "single-phase PDFs", BFO-A represents a mix of BFO-A0.5 and BFO-A2, as the PDF of BFO-A shows atom-pair correlations contained in both other samples (see arrows in Figures S19 and 2g).

Already before any crystallization becomes apparent in the Q-space data (t = −50 s; Figure S17), all three PDFs show correlation lengths to higher r-values with clear features of the phases observed at t = 0 s (see arrows, Figure 2f−h). BFO-A0.5 shows correlations lengths <20 Å (Figure 2f), while BFO-A (Figure 2g) and BFO-A2 (Figure 2h) show correlations >20 Å, suggesting a quicker growth of the $Bi_2Fe_4O_9$ phase. This fits our previous observations, where we observed a gradual $BiFeO_3$ crystallization at lower temperatures for BFO-A0.5 (Figure 1d,g,j) and a sudden $Bi_2Fe_4O_9$ crystallization at higher temperatures for BFO-A and BFO-A2 (Figure 1e,f,k,l).

At t = −100 s, BFO-A and BFO-A2 show only broad bumps <20 Å, characteristic for amorphous materials, although the BFO-A PDF seems to be slightly more structured (compare Figure 2g,h). In contrast, BFO-A0.5 shows clear atom-pair correlations with more intense and distinct features, as highlighted by the green bar in Figure 2f. Remarkably, the PDF at t = −100 s shows even more defined features than the one at t = −50 s, which extend to higher r-values. Thus, although it appears in Q-space that the sample becomes amorphous at 275 °C (Figure 1f), our PDF analysis suggests that it never becomes completely disordered. Instead, the crystalline precursor seems to decompose slowly into the structure observed just before crystallization (t = −50 s). This is evident as we observe the same PDF from 275 °C until $BiFeO_3$ crystallization at 397 °C, only showing a gradual decrease of the correlation length as highlighted in Figure S20. This decomposition product seems to template the crystallization of $BiFeO_3$, which might explain why the observed crystalline gel structure formed in the initial synthesis step determines the later crystallization process.

While the Q-space data suggest that all samples go through an amorphous intermediate, our PDF analysis clearly shows that these intermediates are structurally different. Furthermore, the intermediates even dictate distinct crystallization pathways at higher temperatures, which can be related to specific structural characteristics observed in the PDFs. While the quality of the data does not allow modeling of these intermediates, the structural information seems to be available. It might be extracted when high-quality PDFs with a higher time resolution are available, e.g., from X-ray free-electron lasers (XFEL) that provide extremely short (fs scale) and brilliant radiation pulses.

Our results align with recent studies detailing the importance of the precursor on the phase purity for $BiFeO_3$.[5] A text mining approach was employed by Cruse et al. to extract synthesis parameters affecting the successful production of single-phase $BiFeO_3$ thin films through a sol−gel process. After analyzing 331 synthesis procedures, they highlighted that one of the most important synthesis parameters is associated with the precursor solution preparation.[5] Notably, parameters such as the Bi/Fe ratio and mixing conditions, e.g., time and temperature, emerged as robust predictors of phase purity.[5]

To the best of our knowledge, experimental observation of the influence of the gel and precursor structure on the crystallization pathway, including amorphous intermediates, has not yet been demonstrated. Although the synthesis conditions differ strongly among the five experiments, we consistently observe that a specific structure, formed in the first

https://doi.org/10.1021/acs.chemmater.4c02656
Chem. Mater. XXXX, XXX, XXX−XXX

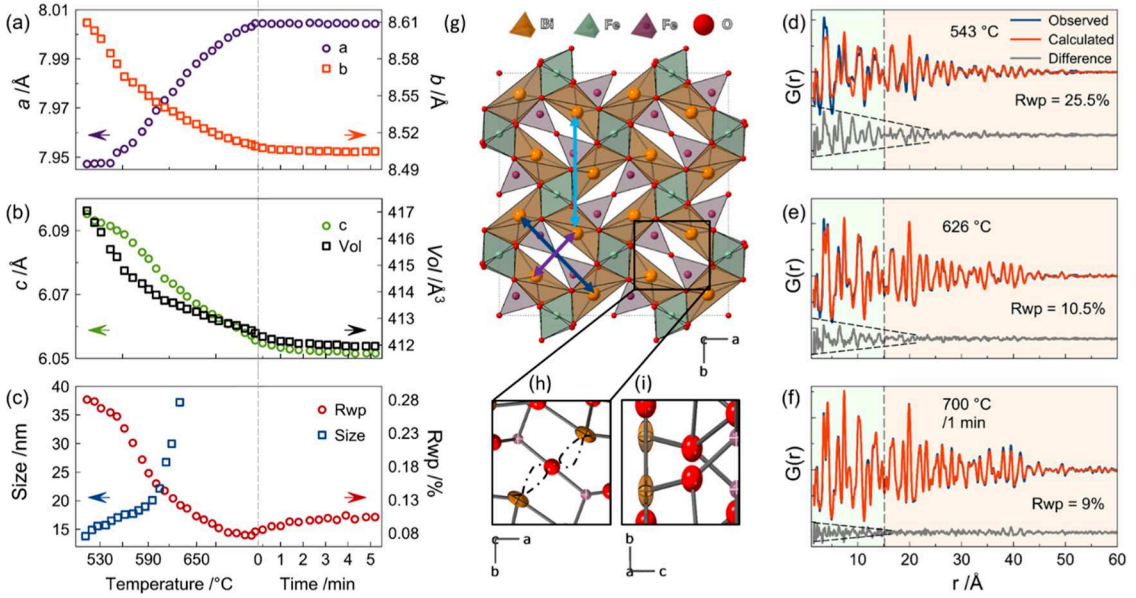

Figure 4. Temperature-dependent evolution of (a) *a* and *b*, (b) *c* and cell volume, and (c) crystallite size and R_{wp} during the growth of $Bi_2Fe_4O_9$ determined by refinements of pair distribution functions (PDF). Of note, for temperatures higher than 629 °C, the crystallites grow too big to be reliably refined, and this parameter was discarded in further refinements. Exemplary refinements of PDF data collected at (d) 543 °C, (e) 626 °C, and (f) 1 min @ 700 °C. The dot−dashed lines are guides to the eye for the local structural distortion correlation length. (g) 2 × 2 supercell of the mullite-type $Bi_2Fe_4O_9$ structure with arrows indicating relevant Bi−Bi pair distances. (h, i) Thermal ellipsoids of Bi in the (h) *ab*-plane and (i) *bc*-plane. The dashed line in panel (h) serves as a guide for the eye for the expression of the $6s^2$ lone electron pair of Bi^{3+}.

step of a sol−gel synthesis, leads to the crystallization of a specific structure later in the process. This remarkable finding suggests that we might be able to finely control the crystallization pathway of compounds from precursors by carefully adjusting the starting solution in a sol−gel synthesis. For example, regarding the synthesis of pure $BiFeO_3$ nanomaterials, we propose that using the synthesis conditions of our BFO-A0.5 sample with the correct Bi:Fe ratio of 1:1 could result in a phase-pure $BiFeO_3$ sample. We assume that because the gel structure, formed under these conditions in our synthesis, favored crystallizing into $BiFeO_3$. Moreover, we recently reported on the synthesis of high-entropy mullite-type oxides by employing the same synthesis parameters as for sample BFO-A2 using D-sorbitol instead of meso-erythritol as a CA.[37] Consistent with the findings in this study, we observed the direct crystallization of the mullite-type structure from an amorphous phase without the emergence of any other crystalline products. The identification of this consistent pathway across diverse samples and compositions supports the conclusion that the initial gel structure indeed plays a pivotal role in dictating the crystallization process. We further speculate that the strong link between the gel structure and the crystallization pathway observed in our study of the $BiFeO_3$-$Bi_2Fe_4O_9$ system could represent a general phenomenon in sol−gel synthesis. However, confirming or disproving this theory will require further research on other systems.

In a broader context, being able to predict the crystallization pathway from the gel structure could allow for more efficient screening of new crystallization pathways and could be a promising way to design new targeted materials. Furthermore, the deliberate manipulation of gel structures through solution chemistry changes presents an auspicious avenue for engineering crystallization pathways, steering them toward or away from metastable intermediates, e.g., for fabrication of nanocomposites or single-phase nanomaterials. In this context, sugar alcohols emerge as particularly advantageous candidates, given their robust metal complexation capabilities, diverse modalities of metal complexation, extensive structural variability in terms of building blocks and stereochemistry, cost-effectiveness, wide accessibility, and low toxicity.

Crystallization of $Bi_2Fe_4O_9$: Dependence of the Crystallite Size on the Structure. We conducted a deeper analysis of the formation and growth process of orthorhombic mullite-type $Bi_2Fe_4O_9$ using sample BFO-A2. The exclusive formation of $Bi_2Fe_4O_9$ allows us to track the detailed evolution of structural features from the point of nucleation to the fully crystalline state. We performed reverse sequential refinements starting from the most crystalline state at high temperatures. To avoid any influence from undescribed amorphous peaks at lower temperatures, we refined the long-range structure within a 15−60 Å range and then kept the parameters fixed when refining the local structure up to 15 Å, as indicated by the orange box in Figure 4d−f. Lattice parameter evolution of *a*, *b*, and *c*, alongside corresponding volume changes, crystallite sizes, and R_{wp} values are shown in Figure 4a−c, respectively. Further refined parameters, such as atomic positions and thermal displacement parameters, are given in Figure S21. Lattice parameter *a* follows the anticipated trend, showing an increase with a higher temperature. On the other hand, *b* and *c* decrease significantly during crystal growth of $Bi_2Fe_4O_9$, resulting in an overall decrease in volume. This deviation from the expected positive thermal expansion reported for $Bi_2Fe_4O_9$[38] is intriguing. Furthermore, it is consistent with prior observations during the growth of other mullite-type materials,[26,37] hinting at a potentially generalized feature within this family of compounds.[37]

The unusual temperature-dependent behavior of the crystal lattice during growth suggests a pronounced size dependence on the structure. This observation aligns with previous research, where substantial size-dependent structural changes

https://doi.org/10.1021/acs.chemmater.4c02656
Chem. Mater. XXXX, XXX, XXX−XXX

in $Bi_2Fe_4O_9$ samples with crystallite sizes less than 121 nm were observed.[26] From our PDF refinements, we observed sluggish crystal growth until ca. 20 nm (~600 °C), beyond which the crystals rapidly grew (Figure 4c). Simultaneously, the cell volume change rate significantly changes (Figure 4b). The smallest size that can reliably be refined is 15 nm (510 °C); at lower temperatures, the R_{wp} increases strongly and we stopped fitting as the $Bi_2Fe_4O_9$ structure model could not describe the PDF anymore (Figure 4c). To the best of our knowledge, no reports of pure $Bi_2Fe_4O_9$ samples with crystals smaller than 15 nm exist in the literature, and extensive efforts by the authors to produce such samples were not successful. This observation suggests a potential instability of the structure beyond this size. Interestingly, two independent studies reported lattice reorientations induced by the electron beam during TEM investigations of $Bi_2Fe_4O_9$ crystals < 10 nm on $BiFeO_3$ surfaces.[13,18]

During crystal growth, the R_{wp} decreases from ca. 28 to 7.6%, after which it slightly increases again to ca. 10% (Figure 4c). This indicates a deviation from the expected mullite-type structure model during the growth, as can also be directly observed by a visual inspection of the PDF peaks in Figures S22, S23, and S24. The PDF peak width and shape significantly change as crystal growth takes place (see arrows in Figure S24).

In our refinements, this broadening is described by increasing the atomic displacement parameters (ADP). We refined the Bi ADPs anisotropically leading to largely elongated thermal ellipsoids in the *ab*-plane at lower temperatures (543 °C, ~17 nm) as seen in Figure 4h,i. The thermal ellipsoid extends minimally in *c*, but stretches significantly in the *ab*-plane, and orients almost parallel to (110). Interestingly, this is orthogonal to the direction where the stereochemically active $6s^2$ lone electron pair (LEP) of Bi^{3+} is pointing into the void of adjacent Fe_2O_7-dimers.[39] Curti et al. have demonstrated that the LEP is important for the stability of the $Bi_2Fe_4O_9$ structure.[39] We notice that with smaller crystallite sizes, the Bi−Bi distances surrounding this void at ca. 4 and 7.5 Å (purple and dark blue arrows, Figure 4g) are gradually changing, decreasing the space for the LEP (Figure S25). As a result, the structure seems to locally distort in the *ab*-plane demonstrated by the large anisotropic ADPs of Bi (Figures 4h,i, and S21i−l). Below 700 °C, we furthermore observe gradual changes in all Fe and Bi positions (Figure S21c,e−h). Bi and the tetrahedrally coordinated Fe simultaneously move together in the *ab*-plane, while the octahedrally coordinated Fe moves in *c*.

The distortion away from the average structure can clearly be seen in the PDF fits in Figure 4d−f. One can observe that the deviations in the difference curve significantly increase with lower temperatures extending further into the higher *r*-region. The fact that the difference curve does not represent the features of the amorphous phase implies that the deviations must be caused by local distortions in the structure, likely involving Bi, as it is by far the strongest scatterer in the sample and therefore dominates the signal. $Bi_2Fe_4O_9$ consists of stiff edge-sharing octahedral chains that are interconnected by Fe_2O_7 dimers and hence is very flexible in the *ab*-plane.[40] As such, it is reasonable to assume that the structure is particularly prone to distortions in the *ab*-plane. In fact, we observe that the Bi−Bi distances associated within the *ab*-plane develop shoulders in the PDFs at lower temperatures (arrows in Figures 4g and S24), clearly demonstrating a more distorted environment. In turn, the Bi−Bi distance at ca. 12 Å associated with adjacent Bi polyhedra in the c-direction does not change much (Figure S24). We propose that the strongly changing distortion in the materials causes the size-dependent properties observed in previous studies and that they are related to the LEPs of Bi. When the distortions get too high, it appears that the Bi atoms surrounding the void move too close to each other, which might cause an instability of the structure below ~15 nm crystallite size.

CONCLUSIONS

Using in situ X-ray total scattering and detailed PDF analysis combined with evolved gas analysis (TGA, MS, and FTIR), we have provided a fundamental understanding of how the formation of $BiFeO_3$ and $Bi_2Fe_4O_9$ nanomaterials can be tuned by using the sol−gel synthesis method. First, we identified that the metal nitrate to the complexing agent ratio influences the crystallization pathways in a sol−gel synthesis and identified three different crystallization routes: (i) decomposition of a crystalline precursor structure into an amorphous intermediate with subsequent crystallization of $BiFeO_3$ and later transition into single-phase $Bi_2Fe_4O_9$, (ii) simultaneous cocrystallization of $BiFeO_3$ and $Bi_2Fe_4O_9$ from a mixed crystalline and amorphous precursor, followed by transition into single-phase $Bi_2Fe_4O_9$, and (iii) direct crystallization of $Bi_2Fe_4O_9$ from an amorphous precursor.

We then applied PDF analysis to the products formed in the early stages of the synthesis, i.e., after solvent evaporation (gel) and prior calcination (precursor) to gain mechanistic insights. We discovered that the structural entities obtained during gel formation cause distinct crystallization pathways and direct the crystallization process from the very beginning. By in situ PDF analysis of data collected during calcination, we observe that the precursors decompose into different amorphous intermediates during heating, showing distinguishable structural features. By coupling these results to TGA-MS, we can rationalize the decomposition of precursors and crystallization into either $BiFeO_3$ or $Bi_2Fe_4O_9$, as these events have very distinct CO_2, NO_x, and H_2O releases.

Our study thus shows that even with a fixed Bi/Fe stoichiometry, the formation pathways in the $BiFeO_3$−$Bi_2Fe_4O_9$ system can be tuned through sole adjustments of synthesis conditions. By preparing a suitable precursor, the crystallization of compounds stable at lower temperatures (here, $BiFeO_3$) can be bypassed. As such, we could study the crystallization of $Bi_2Fe_4O_9$ in depth and find that its unusual crystal growth behavior can be explained by Bi displacement at smaller crystallite sizes. Below 15 nm, the lone electron pairs of Bi^{3+} get too close to each other, causing an instability of the structure for small nanocrystallites.

This study further demonstrates the importance of mechanistic studies on materials formation as they can help in the design of materials with specific structural features. In situ PDF analysis allows one to distinguish between structures appearing as simply amorphous in conventional X-ray diffraction. Furthermore, detailed structural analysis of data collected during the growth of materials can point to interesting phenomena in the nanoregime, which might be hidden in an unusual growth behavior of the material as demonstrated for $Bi_2Fe_4O_9$.

https://doi.org/10.1021/acs.chemmater.4c02656
Chem. Mater. XXXX, XXX, XXX−XXX

■ ASSOCIATED CONTENT

Supporting Information

The Supporting Information is available free of charge at https://pubs.acs.org/doi/10.1021/acs.chemmater.4c02656.

Experimental methods, refinement strategy, and further PDF, XRD, FTIR, and TGA/MS/IR data (PDF)

■ AUTHOR INFORMATION

Corresponding Authors

Andrea Kirsch − *Department of Chemistry and Nanoscience Center, University of Copenhagen, 2100 Copenhagen Ø, Denmark;* orcid.org/0000-0003-2602-7415; Email: anki@chem.ku.dk

Kirsten M. Ø. Jensen − *Department of Chemistry and Nanoscience Center, University of Copenhagen, 2100 Copenhagen Ø, Denmark;* orcid.org/0000-0003-0291-217X; Email: kirsten@chem.ku.dk

Authors

Guilherme B. Strapasson − *Department of Chemistry and Nanoscience Center, University of Copenhagen, 2100 Copenhagen Ø, Denmark; Institute of Chemistry, University of Campinas, UNICAMP, Campinas, SP 13083-970, Brazil; Brazilian Synchrotron Light Laboratory, CNPEM, Campinas, SP 13083-100, Brazil;* orcid.org/0000-0003-2122-679X

Niels Lefeld − *University of Bremen, Institute of Inorganic Chemistry and Crystallography, D-28359 Bremen, Germany; PETRA III, Deutsches Elektronen-Synchrotron (DESY), 22607 Hamburg, Germany*

Mathias Gogolin − *University of Bremen, Institute of Inorganic Chemistry and Crystallography, D-28359 Bremen, Germany*

Mark C. Videbæk − *Department of Chemistry and Nanoscience Center, University of Copenhagen, 2100 Copenhagen Ø, Denmark*

Soham Banerjee − *PETRA III, Deutsches Elektronen-Synchrotron (DESY), 22607 Hamburg, Germany;* orcid.org/0000-0001-9271-493X

Heloisa N. Bordallo − *Niels Bohr Institute, University of Copenhagen, 2100 Copenhagen Ø, Denmark;* orcid.org/0000-0003-0750-0553

Complete contact information is available at: https://pubs.acs.org/10.1021/acs.chemmater.4c02656

Notes

The authors declare no competing financial interest.

■ ACKNOWLEDGMENTS

This work is part of a project that has received funding from the European Research Council (ERC) under the European Union's Horizon 2020 Research and Innovation Programme (Grant Agreement No. 804066). The authors are grateful to the Villum Foundation for financial support through a Villum Young Investigator Grant (VKR00015416). Funding from the Danish Ministry of Higher Education and Science through the SMART Lighthouse is gratefully acknowledged. The authors acknowledge support from the Danish National Research Foundation Center for High-entropy Alloy Catalysis (DNRF 149). The Danish Research Council is acknowledged for covering travel expenses in relation to the synchrotron experiment (DanScatt). A.K. gratefully acknowledges the Deutsche Forschungsgemeinschaft (DFG, German science foundation) for funding of the project Ki 2427/1-1 (# 429360100). G.B.S. gratefully acknowledges Fundação de Amparo à Pesquisa do Estado de São Paulo (FAPESP 2018/01258-5, 2020/12986-1, and 2023/02561-1) and Coordenação de Aperfeiçoamento de Pessoal de Nível Superior (CAPES finance code 001) for funding, and Prof. Dr. Daniela Zanchet and Dr. Cristiane B. Rodella for supervision. The authors acknowledge DESY (Hamburg, Germany), a member of the Helmholtz Association HGF, for the provision of experimental facilities. Parts of this research were carried out at PETRA III beamline P21.1. The authors also thank Dr. Ann-Christin Dippel for helping with the design and fabrication of the sample holder for the beamtime. Beamtime was allocated for proposal I-20200535. The thermal analysis apparatus was financed by Carlsberg Foundation (CF21-0308, 2013_01_0589, CF14-0230, and CF20-0130).

■ REFERENCES

(1) Niederberger, M. Nonaqueous Sol−Gel Routes to Metal Oxide Nanoparticles. *Acc. Chem. Res.* **2007**, *40* (9), 793−800.

(2) Danks, A. E.; Hall, S. R.; Schnepp, Z. The Evolution of 'Sol−Gel' Chemistry as a Technique for Materials Synthesis. *Mater. Horiz.* **2016**, *3* (2), 91−112.

(3) Baig, N.; Kammakakam, I.; Falath, W. Nanomaterials: A Review of Synthesis Methods, Properties, Recent Progress, and Challenges. *Mater. Adv.* **2021**, *2* (6), 1821−1871.

(4) Mackenzie, J. D.; Bescher, E. P. Chemical Routes in the Synthesis of Nanomaterials Using the Sol−Gel Process. *Acc. Chem. Res.* **2007**, *40* (9), 810−818.

(5) Cruse, K.; Baibakova, V.; Abdelsamie, M.; Hong, K.; Bartel, C. J.; Trewartha, A.; Jain, A.; Sutter-Fella, C. M.; Ceder, G. Text Mining the Literature to Inform Experiments and Rationalize Impurity Phase Formation for $BiFeO_3$. *Chem. Mater.* **2024**, *36* (2), 772−785.

(6) Cheetham, A. K.; Mellot, C. F. In Situ Studies of the Sol-Gel Synthesis of Materials. *Chem. Mater.* **1997**, *9* (11), 2269−2279.

(7) Fan, F.; Feng, Z.; Li, C. UV Raman Spectroscopic Studies on Active Sites and Synthesis Mechanisms of Transition Metal-Containing Microporous and Mesoporous Materials. *Acc. Chem. Res.* **2010**, *43* (3), 378−387.

(8) Walton, R. I. Perovskite Oxides Prepared by Hydrothermal and Solvothermal Synthesis: A Review of Crystallisation, Chemistry, and Compositions. *Chem. - Eur. J.* **2020**, *26* (42), 9041−9069.

(9) Chen, B. R.; Sun, W.; Kitchaev, D. A.; Mangum, J. S.; Thampy, V.; Garten, L. M.; Ginley, D. S.; Gorman, B. P.; Stone, K. H.; Ceder, G.; Toney, M. F.; Schelhas, L. T. Understanding Crystallization Pathways Leading to Manganese Oxide Polymorph Formation. *Nat. Commun.* **2018**, *9* (1), No. 2553.

(10) Sun, W.; Kitchaev, D. A.; Kramer, D.; Ceder, G. Non-Equilibrium Crystallization Pathways of Manganese Oxides in Aqueous Solution. *Nat. Commun.* **2019**, *10* (1), No. 573.

(11) Jensen, K. M. Ø.; Andersen, H. L.; Tyrsted, C.; Bøjesen, E. D.; Dippel, A.-C.; Lock, N.; Billinge, S. J. L.; Iversen, B. B.; Christensen, M. Mechanisms for Iron Oxide Formation under Hydrothermal Conditions: An in Situ Total Scattering Study. *ACS Nano* **2014**, *8* (10), 10704−10714.

(12) Juelsholt, M.; Aalling-Frederiksen, O.; Christiansen, T. L.; Kjær, E. T. S.; Lefeld, N.; Kirsch, A.; Jensen, K. M. Ø. Influence of the Precursor Structure on the Formation of Tungsten Oxide Polymorphs. *Inorg. Chem.* **2023**, *62* (37), 14949−14958.

(13) Ortiz-Quiñonez, J. L.; Díaz, D.; Zumeta-Dubé, I.; Arriola-Santamaría, H.; Betancourt, I.; Santiago-Jacinto, P.; Nava-Etzana, N. Easy Synthesis of High-Purity $BiFeO_3$ Nanoparticles: New Insights Derived from the Structural, Optical, and Magnetic Characterization. *Inorg. Chem.* **2013**, *52* (18), 10306−10317.

(14) Han, H.; Lee, J. H.; Jang, H. M. Low-Temperature Solid-State Synthesis of High-Purity $BiFeO_3$ Ceramic for Ferroic Thin-Film Deposition. *Inorg. Chem.* **2017**, *56* (19), 11911−11916.
(15) Kim, J. K.; Kim, S. S.; Kim, W.-J. Sol−Gel Synthesis and Properties of Multiferroic $BiFeO_3$. *Mater. Lett.* **2005**, *59* (29−30), 4006−4009.
(16) Catalan, G.; Scott, J. F. Physics and Applications of Bismuth Ferrite. *Adv. Mater.* **2009**, *21* (24), 2463−2485.
(17) Meera, A. V.; Ganesan, R.; Gnanasekaran, T. Studies on the Thermal Stability of $BiFeO_3$ and the Phase Diagram of Bi-Fe-O System. *J. Alloys Compd.* **2019**, *790*, 1108−1118.
(18) Kirsch, A.; Murshed, M. M.; Schowalter, M.; Rosenauer, A.; Gesing, T. M. Nanoparticle Precursor into Polycrystalline $Bi_2Fe_4O_9$: An Evolutionary Investigation of Structural, Morphological, Optical, and Vibrational Properties. *J. Phys. Chem. C* **2016**, *120* (33), 18831−18840.
(19) Selbach, S. M.; Einarsrud, M.-A.; Grande, T. On the Thermodynamic Stability of $BiFeO_3$. *Chem. Mater.* **2009**, *21* (1), 169−173.
(20) Beauvois, K.; Simonet, V.; Petit, S.; Robert, J.; Bourdarot, F.; Gospodinov, M.; Mukhin, A. A.; Ballou, R.; Skumryev, V.; Ressouche, E. Dimer Physics in the Frustrated Cairo Pentagonal Antiferromagnet $Bi_2Fe_4O_9$. *Phys. Rev. Lett.* **2020**, *124* (12), No. 127202.
(21) Li, Y.; Zhang, Y.; Ye, W.; Yu, J.; Lu, C.; Xia, L. Photo-to-Current Response of $Bi_2Fe_4O_9$ Nanocrystals Synthesized through a Chemical Co-Precipitation Process. *New J. Chem.* **2012**, *36* (6), 1297−1300.
(22) Zhang, Q.; Gong, W.; Wang, J.; Ning, X.; Wang, Z.; Zhao, X.; Ren, W.; Zhang, Z. Size-Dependent Magnetic, Photoabsorbing, and Photocatalytic Properties of Single-Crystalline $Bi_2Fe_4O_9$ Semiconductor Nanocrystals. *J. Phys. Chem. C* **2011**, *115*, 25241−25246.
(23) Wang, Y.; Daboczi, M.; Mesa, C. A.; Ratnasingham, S. R.; Kim, J. S.; Durrant, J. R.; Dunn, S.; Yan, H.; Briscoe, J. $Bi_2Fe_4O_9$ Thin Films as Novel Visible-Light-Active Photoanodes for Solar Water Splitting. *J. Mater. Chem. A* **2019**, *7* (16), 9537−9541.
(24) Singh, A. K.; Kaushik, S. D.; Kumar, B.; Mishra, P. K.; Venimadhav, A.; Siruguri, V.; Patnaik, S. Substantial Magnetoelectric Coupling near Room Temperature in $Bi_2Fe_4O_9$. *Appl. Phys. Lett.* **2008**, *92* (13), No. 132910.
(25) Ressouche, E.; Simonet, V.; Canals, B.; Gospodinov, M.; Skumryev, V. Magnetic Frustration in an Iron-Based Cairo Pentagonal Lattice. *Phys. Rev. Lett.* **2009**, *103* (26), No. 267204.
(26) Kirsch, A.; Murshed, M. M.; Litterst, F. J.; Gesing, T. M. Structural, Spectroscopic, and Thermoanalytic Studies on $Bi_2Fe_4O_9$: Tunable Properties Driven by Nano- and Poly-Crystalline States. *J. Phys. Chem. C* **2019**, *123* (5), 3161−3171.
(27) Tian, Z. M.; Yuan, S. L.; Wang, X. L.; Zheng, X. F.; Yin, S. Y.; Wang, C. H.; Liu, L. Size Effect on Magnetic and Ferroelectric Properties in $Bi_2Fe_4O_9$ Multiferroic Ceramics. *J. Appl. Phys.* **2009**, *106* (10), No. 103912.
(28) Park, T.-J.; Papaefthymiou, G. C.; Viescas, A. J.; Moodenbaugh, A. R.; Wong, S. S. Size-Dependent Magnetic Properties of Single-Crystalline Multiferroic $BiFeO_3$ Nanoparticles. *Nano Lett.* **2007**, *7* (3), 766−772.
(29) Selbach, S. M.; Tybell, T.; Einarsrud, M.; Grande, T. Size-Dependent Properties of Multiferroic $BiFeO_3$ Nanoparticles. *Chem. Mater.* **2007**, *19* (26), 6478−6484.
(30) Goebbert, D. J.; Garand, E.; Wende, T.; Bergmann, R.; Meijer, G.; Asmis, K. R.; Neumark, D. M. Infrared Spectroscopy of the Microhydrated Nitrate Ions $NO_3^-(H_2O)_{1-6}$. *J. Phys. Chem. A* **2009**, *113* (26), 7584−7592.
(31) Yang, L.; Hua, X.; Xue, J.; Pan, Q.; Yu, L.; Li, W.; Xu, Y.; Zhao, G.; Liu, L.; Liu, K.; Chen, J.; Wu, J. Interactions between Metal Ions and Carbohydrates. Spectroscopic Characterization and the Topology Coordination Behavior of Erythritol with Trivalent Lanthanide Ions. *Inorg. Chem.* **2012**, *51* (1), 499−510.
(32) Allscher, T.; Klüfers, P.; Mayer, P. Carbohydrate-Metal Complexes: Structural Chemistry of Stable Solution Species. In *Glycoscience*; Fraser-Reid, B. O.; Tatsuta, K.; Thiem, J., Eds.; Springer Berlin Heidelberg: Berlin, Heidelberg, 2008; pp 1077−1139.
(33) Karthik, M.; Faik, A.; Blanco-Rodríguez, P.; Rodríguez-Aseguinolaza, J.; D'Aguanno, B. Preparation of Erythritol−Graphite Foam Phase Change Composite with Enhanced Thermal Conductivity for Thermal Energy Storage Applications. *Carbon* **2015**, *94*, 266−276.
(34) Levitskaia, T. G.; Qafoku, N. P.; Bowden, M. E.; Asmussen, R. M.; Buck, E. C.; Freedman, V. L.; Pearce, C. I. A Review of Bismuth(III)-Based Materials for Remediation of Contaminated Sites. *ACS Earth Space Chem.* **2022**, *6* (4), 883−908.
(35) Anker, A. S.; Christiansen, T. L.; Weber, M.; Schmiele, M.; Brok, E.; Kjær, E. T. S.; Juhás, P.; Thomas, R.; Mehring, M.; Jensen, K. M. Ø. Structural Changes during the Growth of Atomically Precise Metal Oxido Nanoclusters from Combined Pair Distribution Function and Small-Angle X-ray Scattering Analysis. *Angew. Chem., Int. Ed.* **2021**, *60* (37), 20407−20416.
(36) Kang, X.; Chang, Y.; Yang, L.; Xu, Y.; Zhao, G.; Li, S.; Noda, I.; Liu, K.; Chen, J.; Wu, J. Unexpected Deprotonation from a Chemically Inert OH Group Promoted by Metal Ions in Lanthanide−Erythritol Complexes. *Inorg. Chem.* **2021**, *60* (7), 5172−5182.
(37) Kirsch, A.; Bøjesen, E. D.; Lefeld, N.; Larsen, R.; Mathiesen, J. K.; Skjærvø, S. L.; Pittkowski, R. K.; Sheptyakov, D.; Jensen, K. M. Ø. High-Entropy Oxides in the Mullite-Type Structure. *Chem. Mater.* **2023**, *35* (20), 8664−8674.
(38) Murshed, M. M.; Nénert, G.; Burianek, M.; Robben, L.; Mühlberg, M.; Schneider, H.; Fischer, R. X.; Gesing, T. M. Temperature-Dependent Structural Studies of Mullite-Type $Bi_2Fe_4O_9$. *J. Solid State Chem.* **2013**, *197*, 370−378.
(39) Curti, M.; Gesing, T. M.; Murshed, M. M.; Bredow, T.; Mendive, C. B. Liebau Density Vector: A New Approach to Characterize Lone Electron Pairs in Mullite-Type Materials. *Z. Kristallogr. - Cryst. Mater.* **2013**, *228* (12), 629−634.
(40) Friedrich, A.; Biehler, J.; Morgenroth, W.; Wiehl, L.; Winkler, B.; Hanfland, M.; Tolkiehn, M.; Burianek, M.; Mühlberg, M. High-Pressure Phase Transition of $Bi_2Fe_4O_9$. *J. Phys.: Condens. Matter* **2012**, *24* (14), No. 145401.

https://doi.org/10.1021/acs.chemmater.4c02656
Chem. Mater. XXXX, XXX, XXX−XXX